J. Fluid Mech. (2009), *vol.* 630, *pp.* 129–153. © 2009 Cambridge University Press
doi:10.1017/S0022112009006661 Printed in the United Kingdom

Dynamics of laminar separation bubbles at low-Reynolds-number aerofoils

R. HAIN*, C. J. KÄHLER*† AND R. RADESPIEL
Institute of Fluid Mechanics, Technische Universität Braunschweig, 38106 Braunschweig, Germany

(Received 23 November 2007 and in revised form 16 February 2009)

The laminar separation bubble on an SD7003 aerofoil at a Reynolds number $Re = 66\,000$ was investigated to determine the dominant frequencies of the transition process and the flapping of the bubble. The measurements were performed with a high-resolution time-resolved particle image velocimetry (TR-PIV) system. Contrary to typical measurements performed through conventional PIV, the different modes can be identified by applying TR-PIV. The interaction between the shed vortices is analysed, and their significance for the production of turbulence is presented. In the shear layer above the bubble the generation and amplification of vortices due to Kelvin–Helmholtz instabilities is observed. It is found that these instabilities have a weak coherence in the spanwise direction. In a later stage of transition these vortices lead to a three-dimensional breakdown to turbulence.

1. Introduction

In the past, there have been many numerical and experimental investigations of laminar separation bubbles (LSBs). One reason is that these bubbles can have a strong influence on the flow around the aerofoil so that the lift, the drag and the pitching moment are strongly affected. Most typically the pressure drag increases when an LSB appears. The LSBs occur mainly at Reynolds number $Re = 5 \times 10^4, \ldots, 3 \times 10^6$, depending on the aerofoil geometry, the free-stream turbulence level and the like. In this *Re* regime sailplanes and engine turbine blades operate, though in the upper region. In recent years, development of micro air vehicles (MAVs), which operate at $Re \approx 1 \times 10^5$ have led to an increased interest in LSBs. These MAVs may be applied in the future, e.g., to support action forces after a disaster. The wings of the MAVs can be used to produce lift and thrust at the same time by a flapping-and-pitching motion. This is of great interest because the efficiency factor of flapping at low Reynolds numbers is higher than for conventional propulsion by means of a propeller (see Murray & Howle 2003).

In 1966 Gaster investigated pressure-induced LSBs on a flat plate by means of hot-wire anemometry. He mainly investigated the influence of the Reynolds number and the pressure gradient on the LSB. For critical values of these parameters he observed a bubble burst, which referred to an abrupt increase in the bubble length. On aerofoils this effect can lead to a separation of the flow and an instantaneous loss of lift. Horton (1968) investigated the above-mentioned parameters in detail as well.

---

[*] Present address: Institute of Fluid Mechanics and Aerodynamics, Bundeswehr University Munich, 85577 Neubiberg, Germany.

[†] Email address for correspondence: c.kaehler@tu-bs.de

Similar to Owen & Klanfer (1953) he made a distinction between short and long separation bubbles. Accordingly short bubbles only have a local effect on the pressure distribution, and long bubbles have a global influence on the pressure distribution.

Through technical progress more powerful measurement techniques and more computational power are available today. For this reason the scope of the investigations performed in recent years was the mechanism of transition, including the receptivity to oncoming disturbances. The breakdown to turbulence was also the subject of many investigations (see Watmuff 1999; Alam & Sandham 2000; Lang, Rist & Wagner 2004; Marxen, Rist & Wagner 2004). These investigations have led to the following results: The magnitudes of Tollmien–Schlichting (TS) waves are amplified in the attached flow. Due to an adverse pressure gradient the flow separates, and in the separated shear layer the amplification of Kelvin–Helmholtz (KH) instabilities is observed. These KH instabilities lead to a development of three-dimensional vortices in the shear layer and to a breakdown of the laminar shear layer. As a consequence the flow becomes turbulent and reattaches to the aerofoil. The size of the LSB is affected by the initial magnitude of the TS waves. If the magnitude is not prescribed, a so-called flapping of the LSB is observed. The flapping is an up-and-down motion of the separated shear layer (see Spalart & Strelets 2000). For many experimental investigations a forcing of the TS waves is performed in order to avoid the flapping. This leads to a periodic vortex shedding and allows for the application of non-time-resolved measurement technique like the laser Doppler anemometry (LDA) or conventional particle image velocimetry (PIV). Marxen *et al.* (2004) showed that a spanwise modulation of the forcing of the TS waves does not have an influence on the transition scenario.

Recently, Jones, Sandberg & Sandham (2008) performed a direct numerical simulation (DNS) of LSBs on an NACA-0012 aerofoil at $Re = 5 \times 10^4$ and an angle of attack $\alpha = 5°$. The simulations were performed without and with a volume forcing (added disturbance with 0.1 % amplitude) in order to study the influence of the forcing. A strong decrease of the size of the bubble is observed when a forcing is applied. This leads to an improvement of the aerodynamic performance (the lift-to-drag ratio increases by approximately 23 %) while requiring only little energy input. The simulations imply that transition will take place by absolute instability of the two-dimensional vortex shedding within the shear layer in the absence of convectively driven transition.

The influence of a low-frequency disturbance on the LSB was investigated experimentally by Lou & Hourmouziadis (2000). They performed measurements on a flat plate with an induced pressure gradient by means of a bump. In the diffusor of the wind tunnel a rotating flap was mounted to induce periodic velocity oscillations of approximately 13 % of the free-stream velocity in the test section. A bubble formation similar to that of steady flows was found when the flap rotated. However, in comparison to the separation bubble obtained for steady flow conditions, the bubble under unsteady conditions is shorter, although the overall Reynolds number is lower.

Wissink & Rodi (2004) performed DNS of LSBs on a flat plate with different free-stream disturbances. The Reynolds number based on the length of the plate was $Re = 60\,000$. They found the free-stream disturbances to trigger a KH instability. With increasing disturbance the reattachment moved upstream, and the size of the separation bubble was found to be significantly reduced. In addition, a low-frequency flapping of the bubble was observed in the simulations. The reason for this flapping is unknown.

In a large-eddy simulation performed by Wilson & Pauley (1998) without forcing also a bubble flapping was observed. A flat plate with bump above was simulated to induce a pressure gradient. The frequency spectra in the front part of the separation bubble show sharp peaks at a very low frequency (flapping) and at a higher frequency (vortex shedding). With increasing downstream location the peak which corresponds to the flapping vanishes, and the peak which corresponds to the vortex shedding spreads over.

In order to investigate the influence of the test facility on the LSB on an SD7003 aerofoil, Ol *et al.* (2005) performed a comparison between three investigations in different facilities at $Re = 60\,000$ and an angle of attack $\alpha = 4^\circ$. The measurements were done by means of conventional PIV in low-turbulence-level test facilities. Such measurements allow only for the comparison of the time-averaged quantities. The measurements in the different test facilities qualitatively show the main sensitivities of the location of transition and reattachment on the angle of attack, α, or the turbulence level of the facility.

Today, time-resolved measurement techniques are available, which yield access to the velocity field in a two-dimensional plane or even in a three-dimensional volume. In order to resolve the temporal development and spatial formation of an LSB as well as the shed vortices, measurements have been done by Hain & Kähler (2005), Burgmann, Brücker & Schröder (2006) and Hain (2008). Burgmann *et al.* (2006) used the scanning PIV technique to capture the flow field on an SD7003 aerofoil at Reynolds number $Re = 20\,000$. Due to the low sampling rate of the flow field which results from the scanning process, the measurements could not be performed at higher Reynolds numbers. Applying this measurement technique they were able to observe the three-dimensional breakdown to turbulence in the form of C-shaped vortices.

In order to understand the complex flow of an LSB with transition and vortex shedding, the temporal evolution of the flow structures must also be understood. Therefore in the present work time-resolved PIV (TR-PIV) measurements have been performed on an SD7003 aerofoil at a Reynolds number $Re = 66\,000$. The major interest is in the investigation of the existing frequencies in the flow field. Based on a characterization of the oncoming flow, specific spectral contributions to the fluid processes in the LSB are analysed and discussed.

2. Experimental methodology

2.1. *SD7003 aerofoil*

In order to measure the flow of an LSB the SD7003 aerofoil was used. This aerofoil has a relative thickness of $t/c = 8.51\,\%$ and a relative camber of $f/c = 1.46\,\%$, according to Selig, Donovan & Fraser (1989). This aerofoil is specifically designed to operate at Reynolds numbers below 10^5 through the careful layout of adverse pressure gradient regions located ahead of the laminar separation points. Therefore, initial disturbances in the laminar boundary layer are amplified before flow separation, and this keeps the LSB reasonably small.

In order to assess the influence of these initial disturbances and the angle of attack on the LSB, numerous XFoil calculations were performed (Drela 2007). For $\alpha = 4^\circ$ and $Re = 66\,000$ the influence of the turbulence level Tu on the bubble is given in figure 1(a) by means of the friction coefficient c_f. The equation $N = -8.43 - 2.4 \cdot \ln(Tu)$ was applied to get the relation between the turbulence level and N, with N being the exponent from the e^N method from Mack (1977). A significant dependence of the separation bubble length on the turbulence level is observed, although there is no indication of bubble burst. With increasing turbulence levels the bubble length decreases, and the decrease is larger in the rear part of the bubble

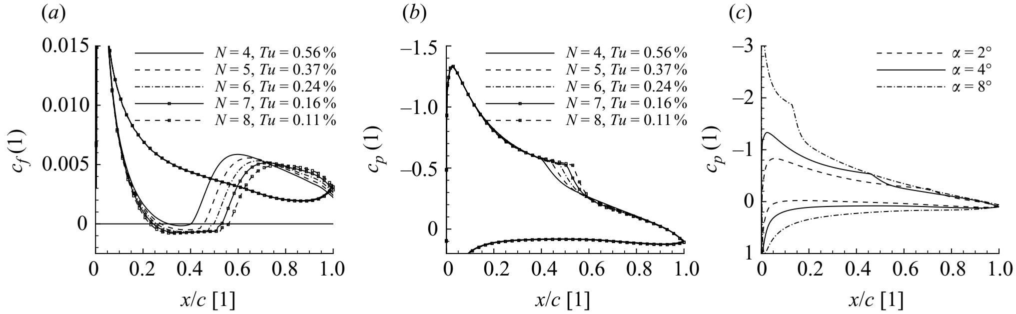

FIGURE 1. Dependence of (*a*) the friction coefficient c_f and (*b*) the pressure coefficient c_p on the turbulence level ($\alpha = 4°$). (*c*) The pressure coefficient c_p for the three investigated angles of attack ($N = 5.5$). The graphs have been calculated by means of XFoil at $Re = 66\,000$.

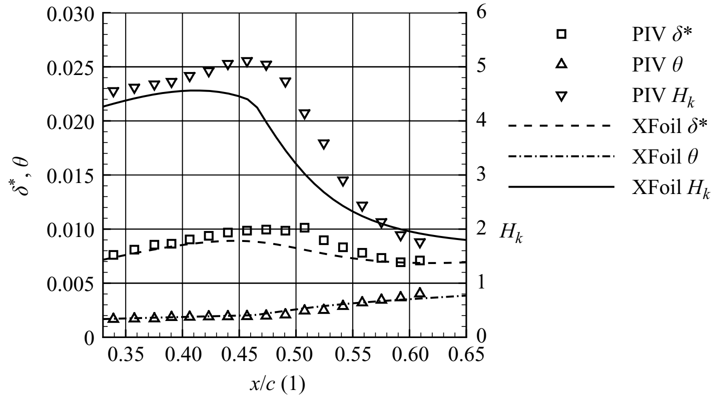

FIGURE 2. Displacement thickness δ^*, momentum-loss thickness θ and shape factor H_k at $\alpha = 4°$. Comparison between the PIV measurement and an XFoil calculation ($N = 5.5$).

than in the front part. The corresponding pressure coefficient for the flow conditions given in figure 1(*a*) is shown in figure 1(*b*). The bump in the pressure distribution which results from the separation bubble is observed in these graphs. With decreasing turbulence level the impact of the bubble on the pressure distribution increases due to the growing bubble length and thickness. It is obvious that the turbulence level must be considered when investigating LSBs. The pressure coefficient c_p is given in figure 1(*c*) for the three investigated angles of attack. With increasing angle of attack the pressure bump induced by the LSB moves upstream and becomes stronger.

For $\alpha = 4°$ the displacement thickness $\delta^\star$, the momentum-loss thickness θ and the shape factor H_k are given in figure 2. A good agreement between the PIV measurement and the XFoil calculation is observed in this figure when considering the values upstream and downstream of the bubble. Both the displacement thickness and the momentum-loss thickness rise to $x/c \approx 0.47$. The displacement thickness decreases slightly in the following region of transition, while the momentum-loss thickness increases strongly. The XFoil calculation shows the same behaviour. However, the position of the separation bubble differs by approximately 2.5 % of the chord length. The variation of the displacement thickness and the momentum-loss thickness occurs at the location at which the flow becomes turbulent (see figure 1). Lift and drag coefficients which have been obtained by means of XFoil calculations are given in

$\alpha(^\circ)$	c_l	c_d
2	0.405	0.015
4	0.606	0.017
8	0.981	0.029

TABLE 1. Lift (c_l) and drag (c_d) coefficients from XFoil calculations.

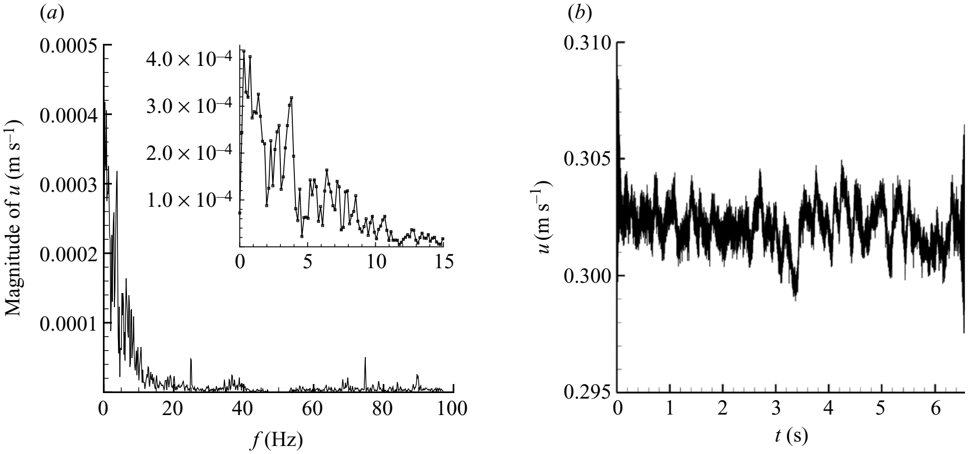

FIGURE 3. Hot-film anemometry measurements of the flow in the water tunnel without an aerofoil inside. The hot-film was located at the position of the leading edge of the aerofoil. (*a*) Fourier spectrum of the velocity signal. The peaks at positions $f = 50 + i \cdot 50,\ i = 0, \ldots, 40$ were set to zero; $U_\infty = 0.31\,\mathrm{m\,s^{-1}}$. (*b*) Reconstructed velocity signal for the calculation of the turbulence level.

table 1 for the investigated angles of attack. For the investigated angles of attack the lift coefficient c_l depends nearly linearly on α.

2.2. *The water tunnel*

The experiments were performed in the water tunnel of the Institute of Fluid Mechanics of the Technical University of Braunschweig. The test section of this tunnel has a length of 1250 mm, width of 250 mm and height of 330 mm and the contraction of the nozzle is 4. As shown in the above section the turbulence level of the test facility is quite important for the investigations presented here. Therefore, the turbulence level of the water tunnel was measured by means of hot-film anemometry. A Fourier spectrum was obtained with a sampling rate of $10^4\,\mathrm{s^{-1}}$ and 65 536 samples (figure 3*a*). The peaks at positions $f = 50 + i \cdot 50,\ i = 0, \ldots, 40$, were set to zero because high electrical disturbances were observed at the multiples of the main frequency. In addition, the frequencies above $2000\,\mathrm{s^{-1}}$ were set to zero because no fluid mechanic disturbances are expected at these high frequencies. The inverse Fourier transform leads to the velocity signal given in figure 3(*b*). At the beginning and the end of the reconstructed sequence, increased magnitudes in the velocity signal are observed. This results from the Fourier transform in which the signal is assumed to be periodic. For the calculation of the turbulence level the 1000 upper and 1000 lower samples are therefore not considered. By means of this procedure the turbulence level in the water tunnel is determined to be $Tu \approx 0.28\,\%$ as an average of eight independent measurements with different sampling frequencies. This corresponds to an N-factor of

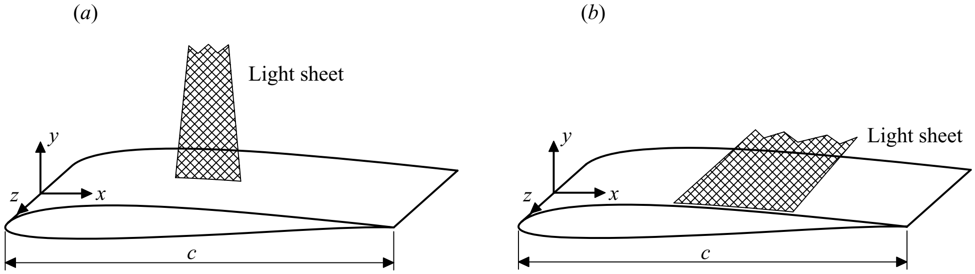

FIGURE 4. (*a*) Sketch of the first experimental set-up. (*b*) Sketch of the second experimental set-up.

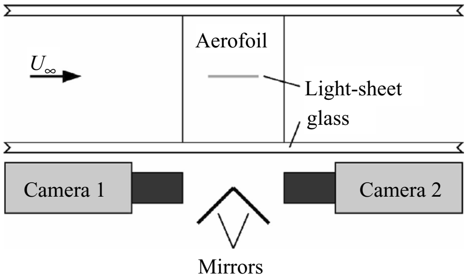

FIGURE 5. Set-up with two high-speed cameras.

approximately 5.5 and thus to a bubble length of $l/c \approx 0.24$ (separation at $x/c \approx 0.256$, reattachment at $x/c \approx 0.497$) in the XFoil calculations. Thus a reasonably large LSB can be expected in the water tunnel, which is well suited for performing optical flow field measurements.

2.3. *Experimental set-up*

For the measurements two experimental set-ups were used. In the first set-up, the light-sheet orientation was parallel to the main flow direction and perpendicular to the aerofoil surface. A sketch of this set-up is shown in figure 4(*a*). The TR-PIV measurements for this set-up with $\alpha = 2^\circ$ and $\alpha = 4^\circ$ were performed with two Redlake HG-100K high-speed cameras with a maximum acquisition frequency of $1000\,\mathrm{s}^{-1}$ at a resolution of $1504 \times 1128\,\mathrm{px}^2$. The Nd:YAG laser LDP-200MQG from Lee was applied for the illumination of the particles. In order to measure the LSB with an even higher spatial resolution, the set-up given in figure 5 was used. The fields of view of the two cameras are both deflected by 90° with the help of two mirrors so that they are facing side by side. For the investigations with $\alpha = 8^\circ$ the same light-sheet orientation was kept, but the hardware from the second experimental set-up with a single camera was used.

In the second experimental set-up, the light-sheet orientation was parallel to the aerofoil surface (see figure 4*b*). In this set-up, the image acquisition was performed with a 1200 hs camera from PCO, allowing a maximum acquisition frequency of $638\,\mathrm{s}^{-1}$ at a resolution of $1280 \times 1024\,\mathrm{px}^2$. A detailed analysis of the cameras was performed by Hain, Kähler & Tropea (2007). A Spectra Physics argon-ion continuous-wave laser 2020-05 with a power of 5 W was used for the particle illumination. In comparison with the high-repetition Nd:YAG laser the argon-ion laser offers a laser beam of much better quality. This leads to a thinner light sheet when the beam is

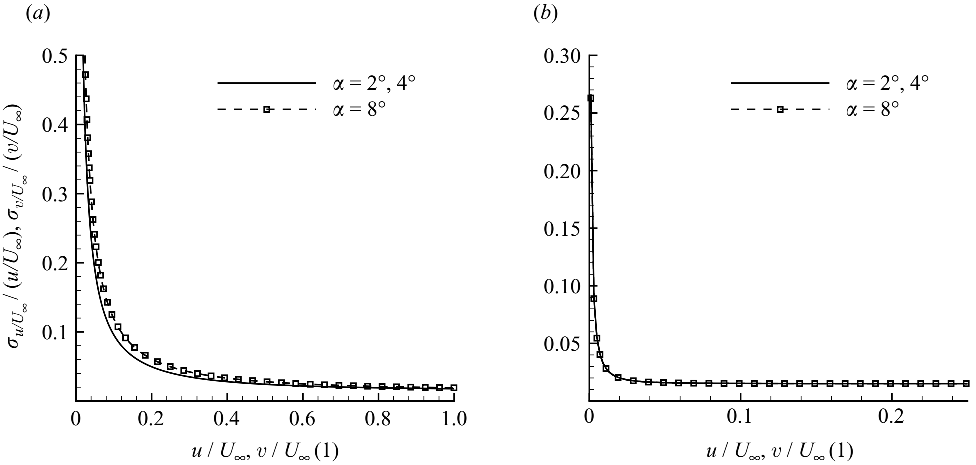

FIGURE 6. (*a*) Measurement error of the normalized velocities for instantaneous flow fields (perpendicular light-sheet orientation). (*b*) Measurement error of the normalized velocities for mean flow fields (perpendicular light-sheet orientation).

focused. Due to the out-of-plane gradients, which occur in this experimental set-up, a thin light sheet is of importance.

Hollow glass spheres with a mean diameter of 10 μm were used as seeding particles. Due to the strong dependence of the viscosity of water on the temperature, the temperature was measured in each experiment, and the velocity of the water tunnel was adapted to get the desired Reynolds number $Re = 66\,000$. This leads to free-stream velocities of approximately $0.33\,\mathrm{ms}^{-1}$. The small gaps between the aerofoil and the tunnel wall of approximately 1 mm were sealed in order to avoid a flow around the tips.

2.4. *Measurement uncertainty*

The accuracy of the TR-PIV measurements shall be discussed here. The normalized velocity in the PIV is calculated by the following equation:

$$\frac{u}{U_\infty} = \Delta X \cdot \frac{M}{\Delta t \cdot U_\infty}. \tag{2.1}$$

There are mainly three errors which must be considered. One is the uncertainty $\sigma_{\Delta X}$ in determining the particle-image displacement ΔX. The second is the uncertainty σ_{U_∞} in determining the free-stream flow velocity U_∞, and the third is the uncertainty σ_M in determining the magnification factor M. The measurement error caused by the uncertainty of the time interval Δt between the laser pulses is neglected due to the relatively large minimum time interval of $\Delta t = 250\,\mu\mathrm{s}$. (Typically this uncertainty is of the order of a few nanoseconds.)

The Gaussian error propagation of (2.1) leads to a measurement error, which is given in figure 6(*a*) for the instantaneous flow fields and in figure 6(*b*) for the mean velocity fields for the perpendicular light-sheet orientation. The uncertainty in determining the particle-image displacement was estimated to be $\sigma_{\Delta X} = 0.1$ px. Therefore a Fourier transformation in time at a vector location was performed. At high frequencies the magnitudes caused by fluid mechanic disturbances are expected to be very small. Therefore these magnitudes must result from the uncertainty in determining the particle-image displacement. Assuming that this uncertainty is white noise in the frequency domain, this noise is equal to the noise in the time domain (for

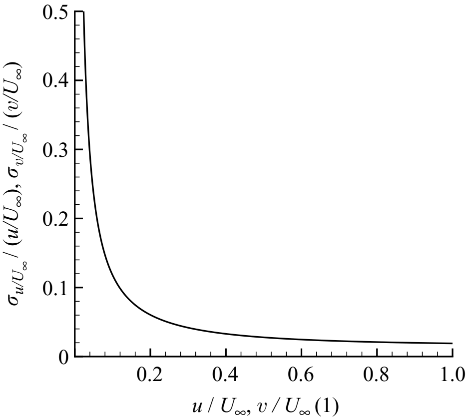

FIGURE 7. Measurement error of the normalized velocities for instantaneous flow fields (parallel light-sheet orientation).

an orthonormal transformation). This error estimation was done at different locations with nearly the same result. As can be seen in figure 6 the error of the mean velocities is smaller than that of the instantaneous velocities. The reason for this is that the uncertainty in determining the particle-image displacement is reduced by the square root of the number of samples when observing the mean velocities.

For the parallel light-sheet orientation, where only instantaneous velocities are considered, the measurement error is given in figure 7.

The error estimation of the statistical fluctuations is much more difficult. Besides the error which results from the uncertainty in determining the particle-image displacement another error occurs due to the averaging over an interrogation window when applying the PIV algorithm. Therefore small-scale fluctuations often cannot be resolved sufficiently. According to Piirto *et al.* (2003) the accuracy of e.g. $u'v'/U_\infty^2$ is typically of the order of 10 % when determined by means of PIV.

The time-resolved measurements offer the possibility to transform the data from the time domain to the frequency domain. The accuracy of the obtained spectrum magnitude is also of interest to evaluate the results. In order to transform the uncertainty in determining the particle-image displacement from the time domain to the frequency domain a simulation was performed. Therefore a sine wave with known magnitude was superimposed with Gaussian noise with a known standard deviation. It was found that this leads to a relative uncertainty of the magnitude in the frequency domain of

$$\frac{\sigma_{m,\ frequency\ domain}}{m_{time\ domain}} = \frac{1.6}{\sqrt{N_{time\ domain}} \cdot SNR_{time\ domain}} \tag{2.2}$$

with $\sigma_{m,\ frequency\ domain}$ being the uncertainty of the magnitude in the frequency domain, $m_{time\ domain}$ being the magnitude in the time domain, $N_{time\ domain}$ being the number of samples in the time domain and $SNR_{time\ domain}$ being the signal-to-noise ratio in the time domain. Considering also the errors caused by σ_M and σ_{U_∞}, the Gaussian error propagation leads to the measurement errors given in figure 8.

3. Results

In this section, the experimental results are presented. All quantities are normalized. The coordinates in physical space are normalized by means of the aerofoil chord

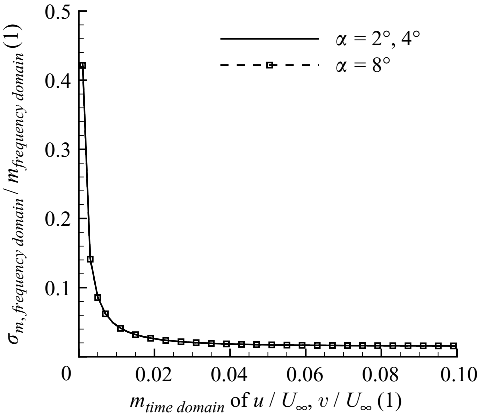

FIGURE 8. Relative magnitude of uncertainty in the frequency domain depending on the magnitude in the time domain.

length c. The Strouhal number Sr is used instead of the frequency:

$$Sr = \frac{f \cdot h_{LSB}}{U_\infty} \tag{3.1}$$

with f being the frequency calculated by means of the Fourier transform and h_{LSB} the maximum thickness of the LSB measured from the aerofoil surface to the maximum of the u-velocity component. In the same manner a normalized time t_{norm} is determined:

$$t_{norm} = \frac{t \cdot U_\infty}{h_{LSB}}. \tag{3.2}$$

In this paper, the $\alpha = 4°$ case is the focus of interest. Selected results for $\alpha = 2°$ and $\alpha = 8°$ are used to indicate that the fluid mechanic processes are not unique to $\alpha = 4°$. The Reynolds number is $Re = 66\,000$.

3.1. *Influence of aspect ratio on the experimental results*

The main measurements were performed on an aerofoil with a chord length $c = 200$ mm. Incorporating the width of the water tunnel of 250 mm leads to an aspect ratio $\Lambda = 1.25$. In order to investigate the influence of this low aspect ratio on the flow around the aerofoil, experiments with an aerofoil with a chord length $c = 100$ mm resulting in an aspect ratio $\Lambda = 2.5$ were also performed. The second experimental set-up (figure 4*b*) was applied for these investigations.

Plots of the normalized mean velocity $\overline{w}/U_\infty$ are given in figure 9 for both the $c = 100$ mm and $c = 200$ mm aerofoils at an angle of attack $\alpha = 4°$. The fields have been calculated from a time-resolved sequence. Therefore the data used for averaging is correlated, and thus some dominant structures are observed. For the $c = 100$ mm aerofoil the vortex shedding frequency is by a factor of 4 higher than the vortex shedding frequency on the $c = 200$ mm aerofoil. This leads to more reliable average velocities for the $c = 100$ mm aerofoil. However, for both aerofoils no strong velocity component $\overline{w}/U_\infty$ towards the aerofoil centre ($z/l = 0.0$) is observed. This means that the effects caused by the wall of the water tunnel are negligible, and the measurements can be performed on an aerofoil with $c = 200$ mm.

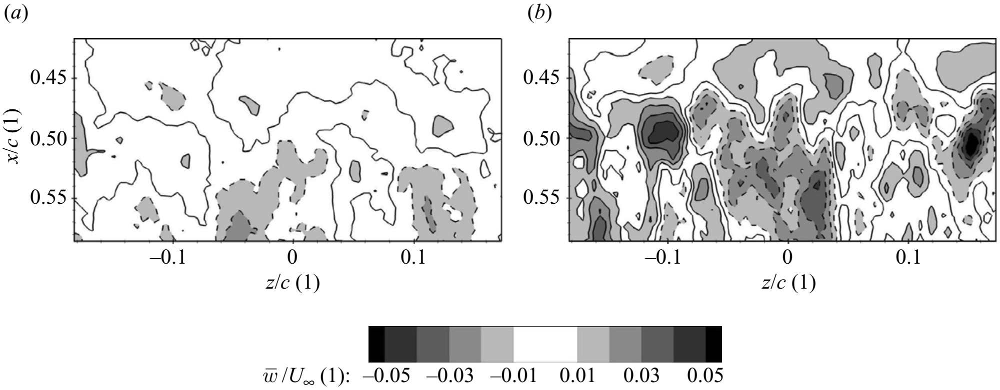

FIGURE 9. $\overline{w}/U_\infty$ in the (x–z)-plane; $\alpha = 4°$. (*a*) Plot for the 100 mm aerofoil. (*b*) Plot for the 200 mm aerofoil.

3.2. *Measurements perpendicular to the aerofoil surface*

These measurements were performed with the set-up shown in figure 4(*a*). The evaluation of the PIV data was performed with DaVis 7.1 from LaVision. For $\alpha = 2°$ and $\alpha = 4°$ the initial interrogation window size was $128 \times 128\,\text{px}^2$, and the final window size was $32 \times 32\,\text{px}^2$ with 50 % overlap. A Gaussian window weighting was applied. The spatial resolution is 0.22 mm based on the vector distance, and the maximum particle-image displacement is $\approx$13 px. The image sequences have each a length of 10.12 s, and 125 double-pair images per second were captured (camera acquisition frequency $250\,\text{s}^{-1}$).

For $\alpha = 8°$ an equidistant image sequence was captured with an acquisition frequency of $1798.5\,\text{s}^{-1}$. This leads to a maximum particle-image displacement of $\approx$15 px. Due to the larger field of view the overlap was set to 75 %, which leads to a resolution of 0.164 mm. The length of the image sequence is 2.25 s. In order to increase the accuracy of the evaluation an advanced multi-frame evaluation approach was applied. Details about this approach can be found in Hain & Kähler (2007).

3.2.1. *Time-averaged fields*

For $\alpha = 4°$ the mean velocity field and shear stresses are given in figures 10 and 11. For comparison, fields measured in the low-noise wind tunnel of the Institute of Fluid Mechanics of the Technical University of Braunschweig are given. This tunnel has a turbulence level of approximately 0.1 %. These measurements were also discussed by Ol *et al.* (2005). The different sizes of the LSBs in both test facilities can clearly be seen in the given figures. Due to the higher turbulence level in the water tunnel the transition occurs upstream, which leads to a separation bubble that is smaller compared with the bubble in the wind tunnel. In the water tunnel the separation takes place at $x/c = 0.35$, the transition at $x/c = 0.45$ (transition criterion is $\overline{-u'v'}/U_\infty^2 = -0.001$). The flow reattaches to the aerofoil at $x/c = 0.53$. The thickness of the separation bubble is $h_{LSB}/c = 0.021$. This thickness is defined as the maximum value of the distances from the aerofoil surface to the maximum $\overline{u}/U_\infty$ in the region of the LSB. In comparison to the data provided by Ol *et al.* (2005) (who applied the same criterion) the bubble is thinner and shorter. The separation in the water tunnel occurs downstream, while transition and reattachment are observed upstream. From this comparison it is also observed that the maximum turbulent shear stress in the

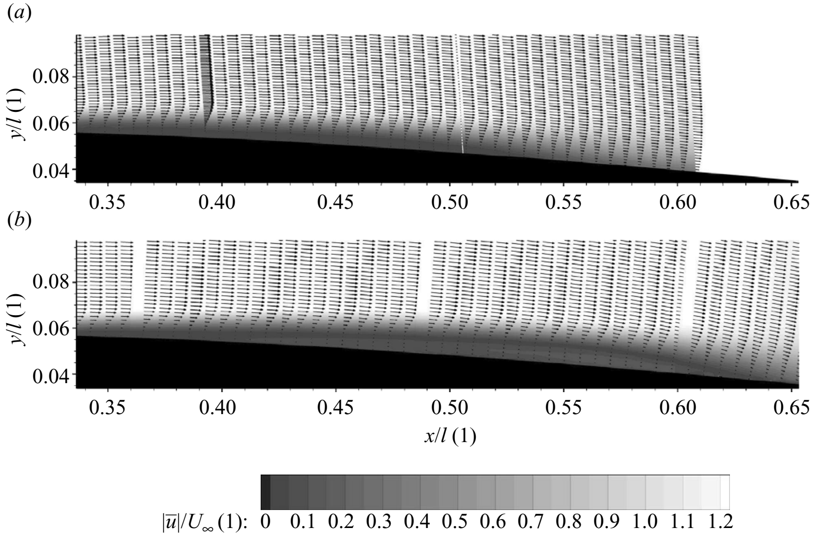

FIGURE 10. Mean velocity fields obtained from measurements in (a) the water tunnel and (b) the wind tunnel at an angle of attack $\alpha = 4^\circ$.

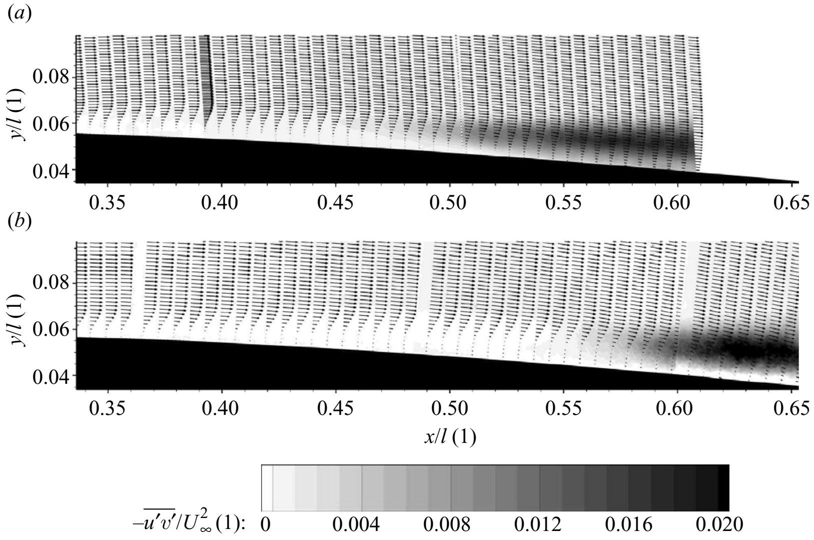

FIGURE 11. Shear stress obtained from measurements in (a) the water tunnel and (b) the wind tunnel at an angle of attack $\alpha = 4^\circ$.

wind tunnel is larger than in the water tunnel. It is assumed that this results from the larger separation bubble in the wind tunnel. This leads to stronger shed vortices and thus to a higher shear stress.

In table 2 some characteristic locations are given for the investigated angles of attack. With increasing angle of attack the bubble becomes shorter and moves upstream. This is typical of short bubbles as already found by Horton (1968). The bubble thickness decreases with increasing angle of attack.

α (°)	Separation (x/c)	Transition (x/c)	Reattachment (x/c)	Bubble thickness (h_{LSB}/c)
2	0.55	0.68	0.77	0.027
4	0.35	0.45	0.53	0.021
8	0.078	0.147	0.205	0.016

TABLE 2. Characteristics of the LSB at several angles of attack.

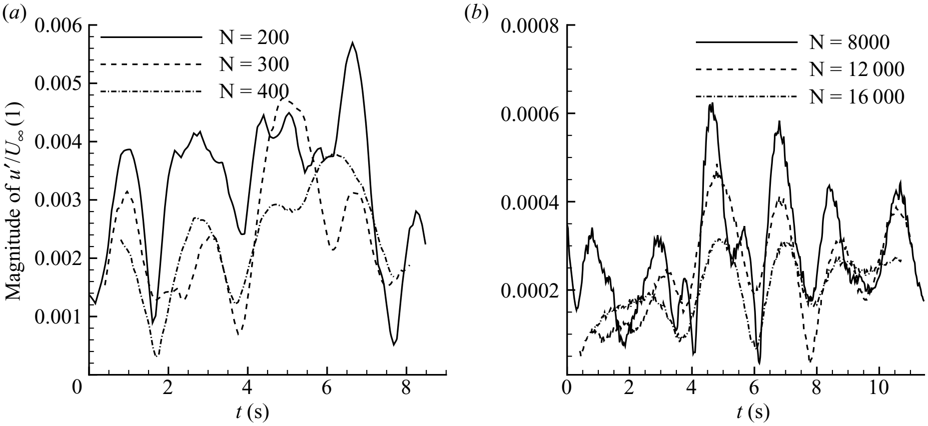

FIGURE 12. (*a*) Magnitude at $Sr = 0.136$ ($f = 10.67\,\text{s}^{-1}$) depending on the time for $\alpha = 4°$ at location $x/c = 0.33$, $y/c = 0.0587$ (PIV measurement). (*b*) Magnitude at $f = 10.67\,\text{s}^{-1}$ as a function of the time (measurement was performed through hot-film anemometry without an aerofoil in the test section).

3.2.2. *Oncoming flow and boundary-layer instabilities*

From other experimental and numerical investigations it is well known that disturbances in the oncoming flow have an influence on the separation bubble (see e.g. figure 1*a*). Therefore measurements with and without the aerofoil in the test section were performed in order to characterize the oncoming disturbances and to investigate the influence on the flow on the aerofoil.

From a PIV image sequence with a length of 10.12 s the magnitude at $Sr = 0.136$ ($f = 10.67\,\text{s}^{-1}$) is given in figure 12(*a*) as a function of time for location $x/c = 0.33$, $y/c = 0.0587$. As will be seen later, the vortex shedding in the LSB occurs around this Strouhal number. In order to determine the magnitude variation at this frequency, not the whole sequence was used for the Fourier transform. Rather N time steps were applied so that many Fourier transforms of the recorded sequence could be performed (transformation 1: $1, \ldots, N$; transformation 2: $11, \ldots, N + 11$; and so on). The result shows a slight dependence on N. For a large number of N an averaging takes place, and for a small number of N the magnitudes become noisy. However, it is found for all N that a variation of the magnitude with a frequency of approximately $0.5\,\text{s}^{-1}$ takes place. For $\alpha = 4°$ this leads to $Sr = 0.0064$. The conclusion is that the waves occur in packets. In order to answer the question of the origin of the magnitude variation, hot-film anemometry was applied to measure the undisturbed flow in the water tunnel without an aerofoil inside. The same procedure as before leads to the results given in figure 12(*b*). Due to the higher sampling rate, N was multiplied by a factor of 40. In this figure the variation of the magnitude with a

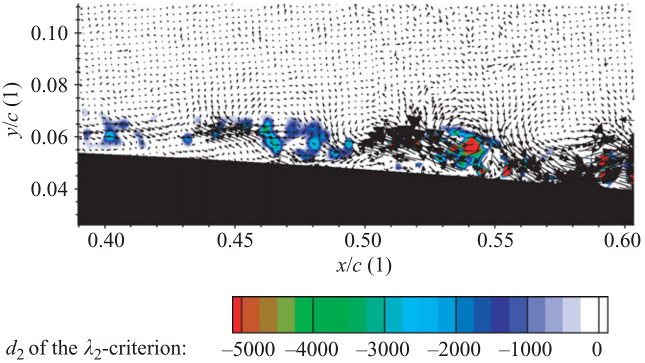

FIGURE 13. Instantaneous flow field for $\alpha = 4°$. The vectors are given by the fluctuation velocities, and the contour colour is given by d_2 from the λ_2-criterion. Every second vector in x- and y-direction is shown.

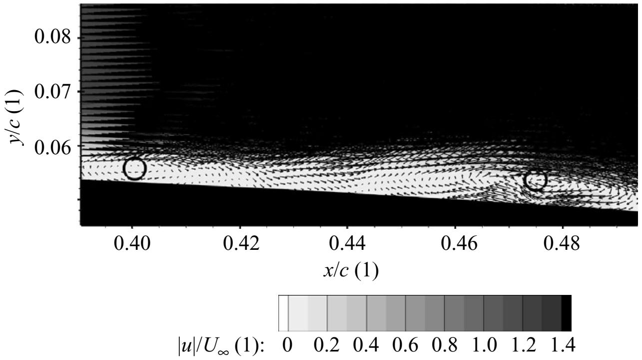

FIGURE 14. Detail of the instantaneous flow field given in figure 13 (real velocities shown, $\alpha = 4°$).

frequency of approximately $0.5\,\mathrm{s}^{-1}$ can also be clearly observed. This indicates a correlation of the disturbances of the oncoming flow with the disturbances observed upstream and in the region of the LSB. The special kind of data analysis applied here shows the magnitude variation at the examined frequency clearly. Using the whole sequence for the Fourier transform (figure 3*a*) an increased magnitude at $f \approx 0.5\,\mathrm{s}^{-1}$ is also observed, but the magnitude variation at a single frequency as a function of the time cannot be determined from such a figure.

3.2.3. *Dynamics of the LSB*

The dynamics of the LSB including transition and vortex shedding shall now be discussed. Instantaneous flow fields of the LSB flow are given in figures 13 and 14. While figure 13 shows the fluctuation velocities and the vortex strength obtained by means of the λ_2-criterion, a detailed view of the real velocities is given in figure 14. Developing vortices are clearly observed in both of these figures. Two vortices which are visible in figure 13 are marked in figure 14 by means of circles. Also in this figure showing the real velocities the vortices can be identified. The vortices seem to have a periodic formation.

While a region with no reverse flow is present between vortices, around $x/c = 0.425, \ldots,\ 0.44$, there is recirculation of the flow in this region in terms of the

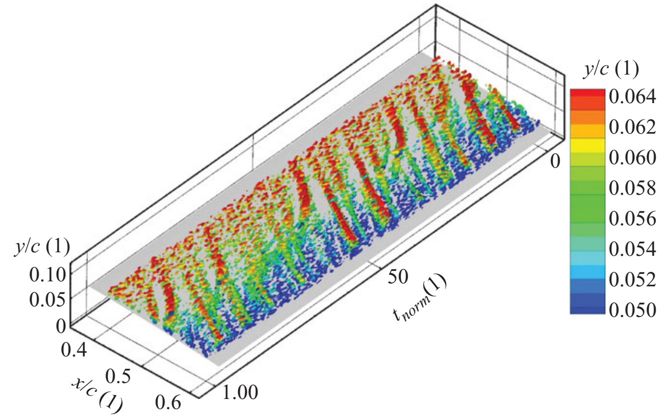

FIGURE 15. Isosurfaces obtained by means of the λ_2-criterion depending on x/c, y/c and the time t_{norm} for $\alpha = 4°$. The normalized d_2 from the λ_2-criterion was set to -1000.

mean velocity field. In figure 13 additional vortices occur above the marked vortices (e.g. $x/c = 0.465$, $y/c = 0.065$). These vortices are results of the velocity fluctuations induced by the primary vortices discussed before. Looking at the distances between the vortices in figure 13, a periodicity of the vortex development is observed. The strength of the fluctuation velocities increases downstream. As was observed in figure 11 this leads to an increase of the shear stress. Downstream of the LSB the large-scale structures break down, and small-scale turbulence increases, leading to a turbulent boundary layer (see Alam & Sandham 2000).

In order to provide more information about the vortex development in the shear layer, the shed vortices are visualized in figure 15 for a longer time period. The λ_2-criterion (Jeong & Hussain 1995) was applied in order to identify the vortices. As shown by Vollmers (2001) this criterion is also suited for analysing flow fields in which only two velocity components are available. The λ_2-criterion is based on the eigenvalues of the velocity-gradient matrix. A negative value of the discriminant d_2 of non-real eigenvalues of the velocity-gradient matrix indicates a vortex. Contrarily to the well-known vorticity, the λ_2-criterion separates shear layers from vortices. The periodicity of the vortex shedding is clearly observed in figure 15. At the beginning of the displayed sequence three vortices with nearly constant convection velocity are visible. After these vortices, another vortex with a decreasing convection velocity is observed. This vortex moves downward and vanishes. The following vortices also have a nearly constant convection velocity followed by a vanishing vortex. From $x/c \approx 0.51$ on an increase of the noise is observed (small clusters of iso-d_2 surfaces). This is a result from the breakdown to turbulence. However, the vortices identified by means of the λ_2-criterion are still present.

For $\alpha = 2°$ (figure 16) the result is quite similar. The formation of the vortices at $x/c \approx 0.62$ is clearly visible, and in addition the vanishing vortices are observed. For $\alpha = 8°$ an increase in the periodicity is observed (see figure 17). In addition the vortex strength increases significantly.

In order to identify the frequency of these vortices, a Fourier transform in time was performed at every vector location. From these Fourier transforms, the dominant frequency at each vector location was determined. The dominant frequency is defined as the frequency with the largest magnitude. The result is shown in figure 18(a,b) for $\alpha = 4°$. The Fourier transform was performed separately for u'/U_∞ and v'/U_∞.

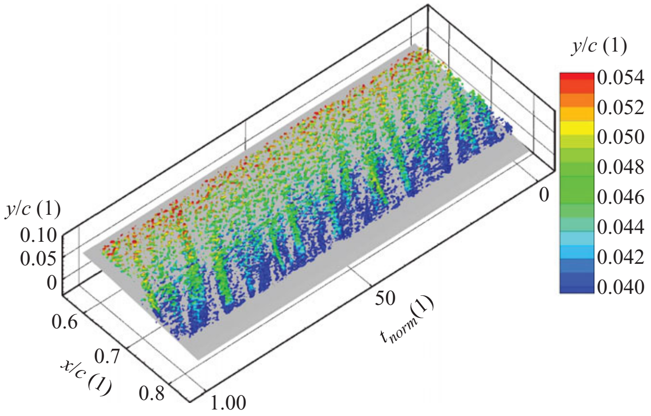

FIGURE 16. Isosurfaces obtained by means of the λ_2-criterion depending on x/c, y/c and the time t_{norm} for $\alpha = 2^{\circ}$. The normalized d_2 from the λ_2-criterion was set to -1000.

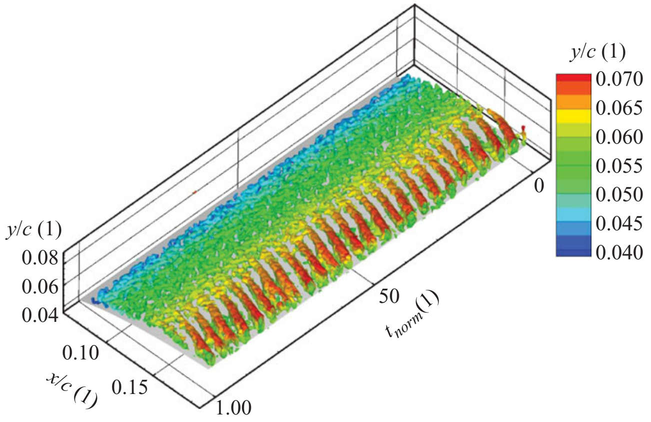

FIGURE 17. Isosurfaces obtained by means of the λ_2-criterion depending on x/c, y/c and the time t_{norm} for $\alpha = 8^{\circ}$. The normalized d_2 from the λ_2-criterion was set to -5000.

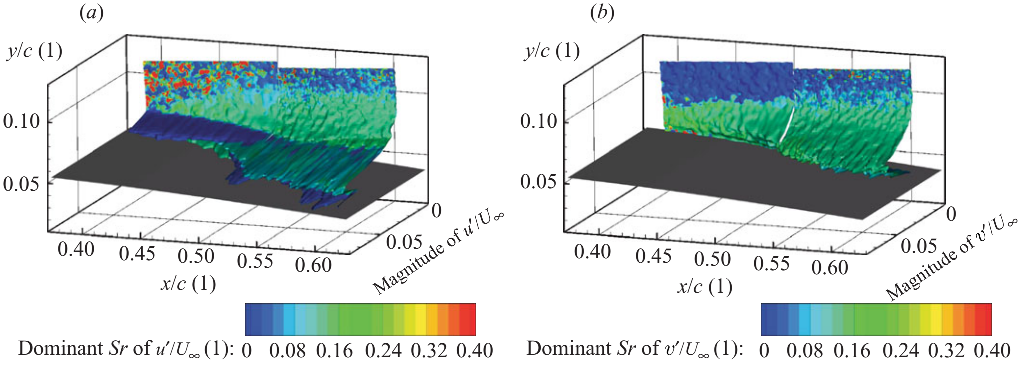

FIGURE 18. Dominant Strouhal numbers for $\alpha = 4^{\circ}$; (*a*) u'/U_{∞}, (*b*) v'/U_{∞}.

For u'/U_∞ different regions can be identified. Near the aerofoil a region with a Strouhal number $Sr = 0.0064$ and a decreasing magnitude is visible. For $\alpha = 4^\circ$ this Strouhal number is equivalent to $0.5\,\mathrm{s}^{-1}$. This variation of the magnitude at $10.67\,\mathrm{s}^{-1}$ with a frequency of $0.5\,\mathrm{s}^{-1}$ was already observed in the undisturbed oncoming flow. Beginning at $x/c \approx 0.46$ a second region with an increasing magnitude and $Sr \approx 0.1$ occurs. A third wedge-shaped region starts at $x/c \approx 0.4$ with $Sr \approx 0.13$. For v'/U_∞ only one region is observed beginning at $x/c \approx 0.4$ with $Sr \approx 0.13$. This region is quite similar to the third region of u'/U_∞. The Strouhal number $Sr \approx 0.13$ is of the order of the vortex shedding, which was observed in figure 15. This indicates that the vortex shedding is the dominant process. From figures 3(*a*) and 12(*b*) it can be derived that the disturbances in the oncoming flow at the frequency $f = 10.67\,\mathrm{s}^{-1}$ are of the order of 0.03 % of the free-stream velocity. Thus, the magnitude of these disturbances which may trigger the KH instabilities are well below the free-stream turbulence level of 0.28 %. However, DNSs from Marxen *et al.* (2004) show that magnitudes of the order of 0.05 % of the free-stream velocity do have an influence on the flow. In these simulations the forcing leads to a more stable vortex shedding and avoids a bubble flapping. Jones *et al.* (2008) showed by means of DNS of the flow on an NACA-0012 aerofoil that an amplitude of a disturbance of 0.1 % of the free-stream velocity strongly influences the LSB. The bubble becomes shorter, and the location of reattachment moves upstream. Although the amplitude of the disturbance in the experiment presented here is much smaller, it may be sufficient to reduce the size of the bubble compared to measurements given by Ol *et al.* (2005). A variation of the magnitude at $f = 10.67\,\mathrm{s}^{-1}$ as observed here would lead to growing and shrinking of the bubble, resulting in the bubble flapping.

This assumption is strengthened by numerical calculations from Windte, Scholz & Radespiel (2006). They determined the most unstable frequencies by means of unsteady Reynolds-averaged Navier–Stokes (URANS) calculations with a coupled solver for the linear stability theory. For both the TS waves in the attached shear layer and the KH instabilities in the separated shear layer they found the most unstable frequencies in the range $f \approx 8.5, \ldots, 9.0\,\mathrm{s}^{-1}$ (SD7003, $Re = 60\,000$, $\alpha = 4^\circ$). This is in good agreement with the frequencies found in the experiment presented here. The equality of the most unstable frequencies of the TS waves and the KH instabilities leads to the fact that a modification of the initial magnitude of the TS waves will also modify the magnitude of the KH instability and thus influence the shed vortices and the size of the LSB.

The development of the magnitudes at other Strouhal numbers is shown by using Fourier spectrums for u'/U_∞ and v'/U_∞ in figures 19 and 20 at a fixed x-location. In the temporal mean the transition takes place at this location. For v'/U_∞ different peaks between $Sr = 0.1, \ldots, 0.2$ are observed. The spectrum of u'/U_∞ on the other hand shows additional peaks between $Sr = 0.006, \ldots, 0.1$. The peak at $Sr = 0.0064$ has quite a large magnitude. The reason for this is the so-called flapping of the separation bubble. At location $y/c \approx 0.055$ a line in the spectrum of u'/U_∞ is observed where the magnitudes are small. This location is between the recirculation area and the shear layer above the bubble. Below this location ($y/c = 0.0506, \ldots, 0.055$) a correlation with the streamwise velocity fluctuations at larger y/c-locations is observed. This implies that the flow inside the bubble is strongly influenced by the flow in the shear layer. Furthermore it can be seen that disturbances are amplified not only at a single Strouhal number. In fact, a wide band with large magnitudes is observed. This frequency spectrum shows a good agreement with the results obtained by means of a large-eddy simulation from Wilson & Pauley (1998). In this simulation the flapping

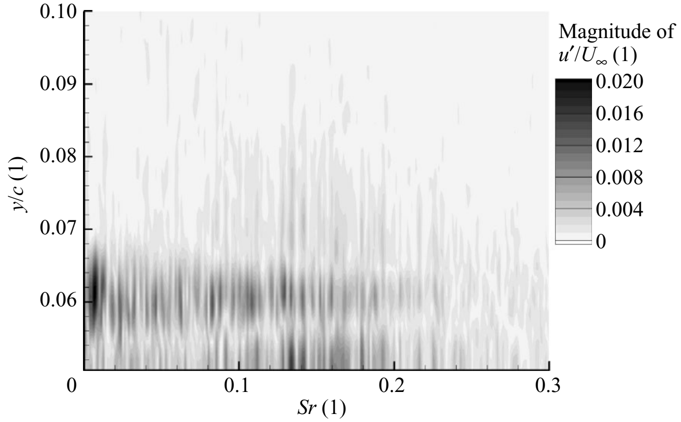

FIGURE 19. Fourier spectrum for u'/U_∞ at location $x/c = 0.45$ ($\alpha = 4^\circ$).

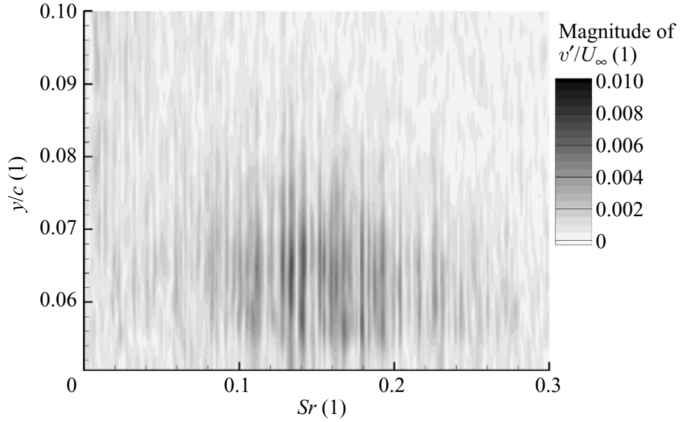

FIGURE 20. Fourier spectrum for v'/U_∞ at location $x/c = 0.45$ ($\alpha = 4^\circ$).

frequency and a region with increased magnitudes resulting from the vortex shedding is observed. The same behaviour was investigated in DNS from Wissink & Rodi (2004). In their simulations on a flat plate at $Re = 60\,000$ (based on the length of the plate) a flapping with a Strouhal number of $Sr = 0.417$ occurs when applying a forcing with $Sr = 12.5$. However, the reason for the flapping in the DNS is unknown. For the measurements presented here, no significant peaks for $Sr > 0.3$ are observed.

The magnitudes of u'/U_∞ and v'/U_∞ for several Strouhal numbers are given in figure 21. In this figure the spatial development of the different modes becomes clear. At $Sr = 0.0064$ and at a distance of approximately $0.01c$ from the aerofoil surface a region with a magnitude of approximately 0.02 is observed for u'/U_∞. For v'/U_∞ the magnitude in this region is close to zero. The reason for this behaviour is the flapping of the separated shear layer, which can be explained as follows: If the velocity gradient $\partial u/\partial y$ is large, a small blade-normal velocity fluctuation leads to a large streamwise velocity fluctuation. The magnitudes at the other Strouhal numbers also have characteristic shapes. For all given Strouhal numbers the blade-normal velocity fluctuations are smaller than the streamwise velocity fluctuations at the same locations. With increasing x/c location a rising magnitude for all given Strouhal numbers is visible for u'/U_∞ at first. After this rise in magnitude a decrease is observed

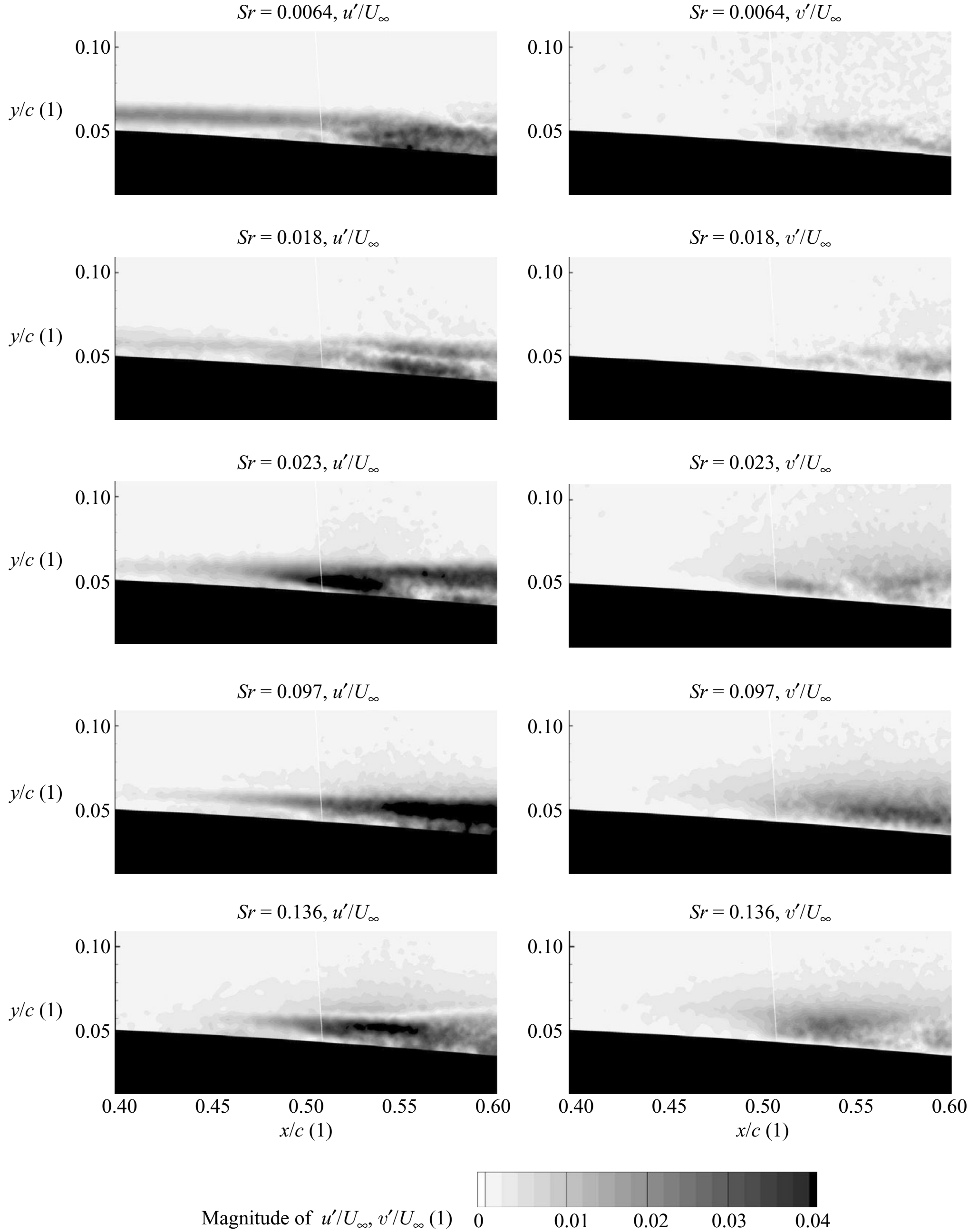

FIGURE 21. Magnitudes of u'/U_∞ and v'/U_∞ for different Strouhal numbers ($\alpha = 4^\circ$).

for some Strouhal numbers (e.g. $Sr = 0.023$, 0.136). For $Sr = 0.136$ the streamwise velocity fluctuation at location $y/c = 0.06$ is quite small. This is not observed for v'/U_∞ at the same location. The reason for this distribution of the magnitudes are the vortices which develop in the shear layer above the separation bubble. When vortices are convected they contribute to a magnitude in v'/U_∞ at the path of the vortex core, but no u'/U_∞ magnitude occurs at this path. This is typical for a KH

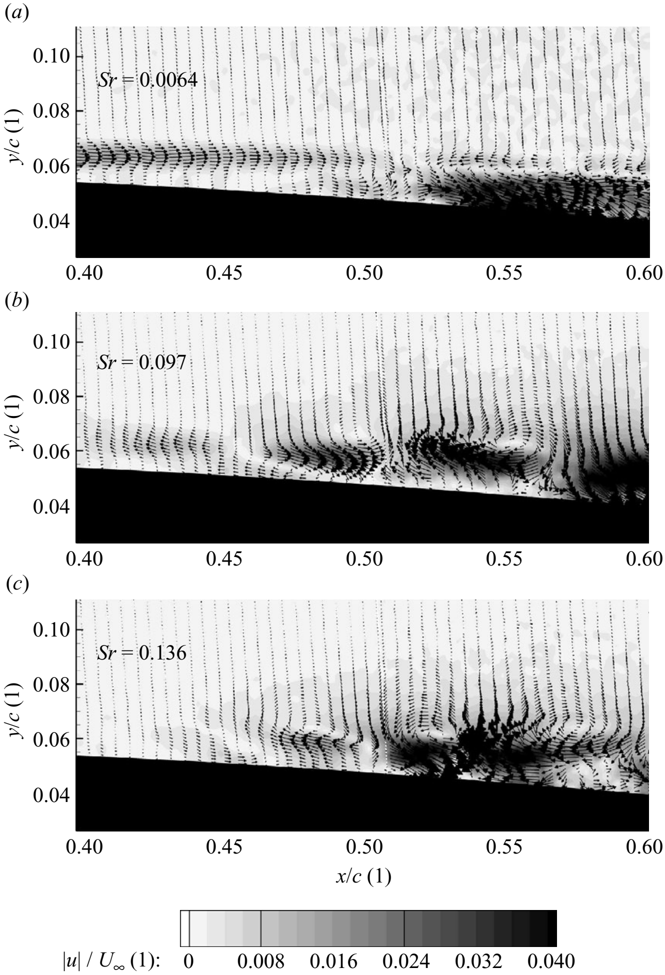

FIGURE 22. Reconstructed vector fields for (*a*) $Sr = 0.0064$, (*b*) $Sr = 0.097$ and (*c*) $Sr = 0.136$ for $\alpha = 4°$.

instability. The resulting eigenfunction of u'/U_∞ has two maxima with a decrease to almost zero in between. The decrease to almost zero also implies that the path of the shed vortices is very similar. For the given Strouhal numbers the streamwise velocity fluctuations become larger in the near-wall region, beginning from $x/c \approx 0.52$. Upstream of this location the magnitudes in the near-wall region are quite small. For the blade-normal velocity fluctuations a wedge-shaped increase is observed. The rise of these magnitudes leads to an increased transport of high-momentum fluid in the wall-normal direction so that the flow reattaches to the aerofoil.

The vortices which develop in the shear layer above the bubble also become visible when the velocity fields for single Strouhal numbers are reconstructed. In figure 22 reconstructed instantaneous velocity fields for selected Strouhal numbers are shown. For the Strouhal number of the flapping ($Sr = 0.0064$) no vortex development is observed. Only velocity fluctuations in the shear layer are visible. The magnitude of the velocity component in the y/c-direction is quite small. Observing the instantaneous fields of the other two Strouhal numbers, the vortex formation

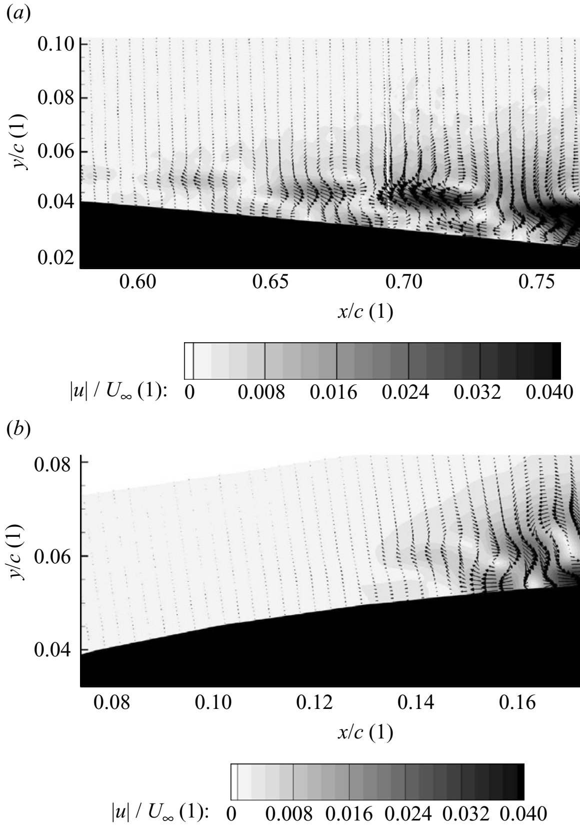

FIGURE 23. Reconstructed vector fields. (*a*) $Sr = 0.149$, $\alpha = 2°$. (*b*) $Sr = 0.25$, $\alpha = 8°$.

in the shear layer becomes clearly visible. The convection velocity of the vortices at $Sr = 0.097$ is approximately 60 % of the free-stream velocity and approximately 57 % for the vortices at $Sr = 0.136$. This is in good agreement with the results obtained by Burgmann *et al.* (2006). With increasing phase the vortices are convected downstream.

For $\alpha = 2°$ and $\alpha = 8°$ reconstructed vector fields are given in figure 23. Again, the vortices which develop in the shear layer due to KH instabilities are observed. For $\alpha = 8°$ the vortex development is only observed for this single Strouhal number.

The reconstructed flow fields at the shown phases are representative of the phenomenons observed. Therefore no additional flow fields at different phases are given here.

The investigations with the light-sheet orientation perpendicular to the aerofoil surface clearly show the periodic development of vortices in the shear layer above the separation bubble. It also becomes apparent that for angles of attack $\alpha = 4°$ and $\alpha = 2°$ only a single fundamental frequency of the vortex shedding is not present. In fact, the velocity signal is composed of several fields with different frequencies. For $\alpha = 8°$ a strong periodicity of the vortex shedding is observed, and the flapping is strongly decreased. The flapping of the bubble is in good agreement with the low-frequency magnitude variation of the disturbances in the oncoming flow (see figure 3*a* and figure 12*b*). Therefore it is likely that the flapping in the performed experiment is correlated with small disturbances in the oncoming flow.

3.2.4. *Transition scenario*

The results presented in the section above lead to the following picture of the transition scenario: The transition is dominated by KH instabilities which cause a vortex growth in the separated shear layer. For $\alpha = 4^\circ$, these instabilities have nearly the same most unstable frequency as the TS instabilities. This leads to a triggering of the amplitudes of the KH instabilities by the amplitudes of the TS waves. From other investigations (Marxen *et al.* 2004; Jones *et al.* 2008) it is well known that a forcing of the TS waves affects the separation bubble. Detailed measurements of the turbulence spectrum in the water tunnel show some peaks that vary in time. For $\alpha = 4^\circ$, such a peak is found at a frequency at which the vortex shedding occurs. The overall turbulence level of the water tunnel is 0.28 %, leading to an N-factor of approximately 6 when applying the formula from Mack (1977).

Computations from Windte *et al.* (2006) show a good agreement between the experiments in the water tunnel and computational fluid dynamics (CFD) results with $N = 7$ for $\alpha = 8^\circ$. For $\alpha = 4^\circ$ a good agreement between the experiment and the computation is found with an N-factor of 6 (Windte 2008, personal communication). This N-factor is also found when comparing the bubble length determined from the experiment (see table 2) to the bubble length determined from the XFoil calculations (figure 1*a*). Thus, the results are consistent, and the N-factor of 6–7 means that no bypass transition occurs. (The limit to bypass transition is often defined as $N = 0$; see Arnal 1994.) Disturbances are amplified according to the linear stability theory.

Obviously, the turbulence which is present in the tunnel has an influence on the transition behaviour. This is expected and nicely shown in Ol *et al.* (2005) and Jones *et al.* (2008). The applied disturbance (according to the turbulence level) leads in these investigations to a variation of the bubble size. In terms of the linear stability theory, the disturbance is a modification of the initial amplitude A_0. Thus, a larger A_0 (or turbulence level) is equivalent to a smaller N. A variation of A_0 in dependence on the time will lead to a bubble flapping as observed in the measurements presented here.

In free-flight conditions, the turbulence level is negligible, and thus no significant turbulence spectrum like in wind/water tunnels is observed. This leads to a high N-factor. However, as shown by Seitz & Horstmann (2006), packets of TS waves are also observed in free-flight conditions. These packets do not have a strong periodicity or a homogeneous size. Their experiments show that TS waves are not strongly two-dimensional. In combination with the results presented here and the paper from Jones *et al.* (2008) such wave packets may lead to a flapping of the bubble also in free-flight conditions (provided that the most unstable frequency from the linear stability theory is near the frequency of the TS waves occurring in packets and that the frequency of the most unstable KH instabilities is also close to this frequency).

3.3. *Measurements parallel to the aerofoil surface*

So far, no information about the vortex shape in the spanwise direction has been obtained. Therefore measurements with the set-up given in figure 4(*b*) were performed. Due to the curvature of the aerofoil the distance of the light sheet was not constant in the x/c-direction. Thus d_{min} is used to characterize the distance of the light sheet from the aerofoil surface (see figure 24). An instantaneous velocity field with $d_{min} = 0.5$ mm is given in figure 25. In this figure, the images of sources and sinks become visible. The incompressible flow which is investigated here must be free of divergence so that a velocity perpendicular to the given plane is the reason for these flow structures. As sketched in figure 26 these sinks and sources result from the vortices which were observed in the measurements with the perpendicular light-sheet orientation.

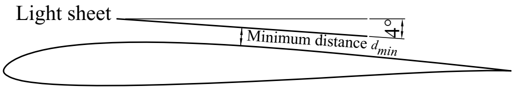

FIGURE 24. Light-sheet adjustment for $\alpha = 4°$.

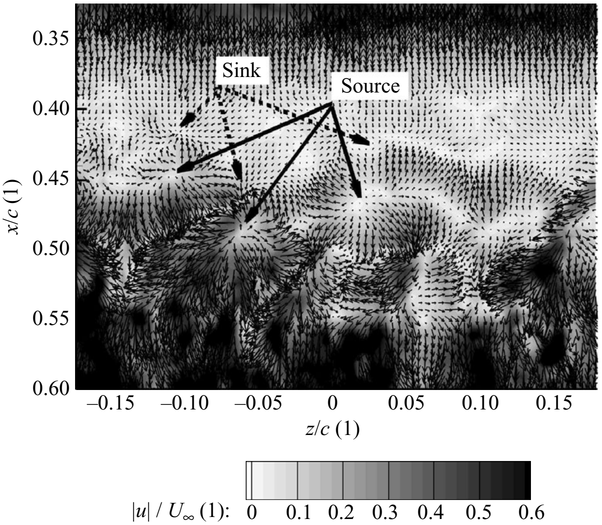

FIGURE 25. Instantaneous velocity field ($\alpha = 4°$, $d_{min} = 0.5$ mm).

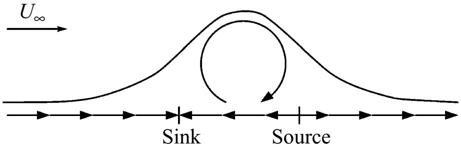

FIGURE 26. Principle of the development of sinks and sources.

In figure 25 the structures are clearly identified, but no regular formation is found. In order to obtain more information about the vortex formation in the spanwise direction, a line $x/c = \text{const.}$ is observed. From such a graph (figure 27*a*) in which the velocity fluctuation u'/U_∞ is shown depending on z/c and t_{norm}, the size of the shed vortices in z/c-direction can also be determined. In figure 27(*a*) the point $x/c = 0.45$ is considered. In the wall-normal measurements this point was determined to be the location of transition. The lengths of the structures in the z/c-direction, which are visible in this figure, are quite different. They lie in the range of $0.05, \ldots, 0.3 \cdot c$ which means that they are larger than the boundary-layer thickness. At the beginning of the given sequence, the structures have a smooth distribution. At the end of the sequence ($t_{norm} = 150, \ldots, 170$) many small-scale fluctuations with increased velocity are observed. The reason must be instantaneous transition upstream from the location $x/c = 0.45$ during this sequence. This early transition leads to a collapse of the regular structures. The structures observed are in good agreement with the results published by Burgmann *et al.* (2006) at $Re = 20\,000$ and $\alpha = 6°$. In figure 27(*a*), a strong variation of the disturbance magnitudes can be seen. Qualitatively this is in good agreement

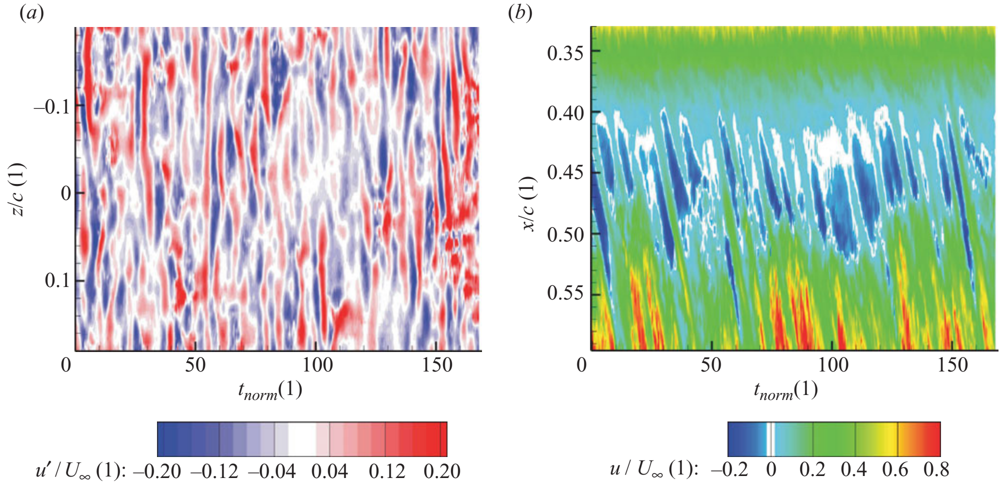

FIGURE 27. (*a*) u'/U_∞ for location $x/c = 0.45$; (*b*) u/U_∞ for location $z/c = 0.0$; $\alpha = 4°$, $d_{min} = 0.5$ mm.

with the observations obtained from the measurements with the wall-normal light-sheet orientation. Due to the length of the sequence of only 2.2 s a quantitative analysis of the variation of the magnitudes is not feasible.

The low-frequency variation of the reattachment location also becomes visible by observing the velocity component u/U_∞ on the line $z/c = 0$ (see figure 27*b*). The convected vortices with their origin at $x/c \approx 0.38$ are clearly visible by means of the velocity fluctuation induced by them. In the area $x/c \approx 0.5$ the sign of u/U_∞ changes. At this location the flow is close to reattachment. After the reattachment the slope of $\partial(x/c)/\partial(t_{norm})$ of the connected velocity regions increases. This implies an increase in the convection velocity of the shed vortices.

4. Summary and conclusion

In this paper TR-PIV measurements on an SD7003 aerofoil at $Re = 66\,000$ were presented to quantitatively estimate the dominant frequencies and magnitudes of the KH instabilities associated with an LSB. It was shown that this technique is well suited for reliably determining frequency spectra. Contrary to other measurement techniques like hot-wire anemometry or LDA which were applied for measurements on LSBs in the past, TR-PIV makes it possible to obtain temporal information for a two-dimensional field. This is of particular interest when the fluid mechanic process is not periodic. In this case flow phenomena are not repeatable, and the information must be captured in a single sequence. This applies to the presented experiment in which no artificial disturbance is introduced to achieve a periodic flow.

The results clearly show that the KH instabilities lead to a vortex formation in the shear layer above the separation bubble. By means of the Fourier transformation a periodicity of the vortex formation was found. Compared to experiments with introduced disturbances (forced TS waves) more than a single vortex shedding frequency was found here. However, dominant structures which lead to large magnitudes in the frequency spectrum were observed. In addition the flapping of the separation bubble was measured. It seems that the flapping in this experiment is associated with a low-frequency variation of the most amplified disturbance. This frequency was also observed in the oncoming flow without the aerofoil in the tunnel.

The investigations with a light sheet aligned nearly parallel to the aerofoil surface gave information about the vortex dimension and interaction in the spanwise direction. The size of the vortices in this direction is in the range $0.05, \ldots, \ 0.3 \cdot c$. A regular formation of the vortices in spanwise direction is not observed, not unlike previous investigations from Burgmann *et al.* (2006) at a lower Reynolds number and from Hain & Kähler (2005) at $Re = 60\,000$.

This research has been supported by the German Research Foundation (DFG) in the priority program SPP 1147 ‘Bildgebende Messverfahren für die Strömungsanalyse’.

REFERENCES

Alam, M. & Sandham, N. D. 2000 Direct numerical simulation of ‘short’ laminar separation bubbles with turbulent reattachment. *J. Fluid Mech.* **410**, 1–28.

Arnal, D. 1994 Boundary layer transition: predictions based on linear theory. *AGARD* **R-793**, 2.1–2.63.

Burgmann, S., Brücker, C. & Schröder, W. 2006 Scanning PIV measurements of a laminar separation bubble. *Exp. Fluids* **41**, 319–326.

Drela, M. 2007 XFoil. http://web.mit.edu/drela/Public/web/xfoil/.

Hain, R. & Kähler, C. J. 2005 Advanced evaluation of time-resolved PIV image sequences. In *Sixth Intl Symp. on Particle Image Velocimetry*, Pasadena, California.

Hain, R. 2008 Untersuchungen zur Dynamik Laminarer Ablöseblasen mit der zeitauflösenolen Particle Image Velocimetry. PhD dissertation, Tu Braunschweig. Shaker Verlag, Aachen, Germany.

Hain, R. & Kähler, C. J. 2007 Fundamentals of multiframe particle image velocimetry (PIV). *Exp. Fluids* **42**, 575–587.

Hain, R., Kähler, C. J. & Tropea, C. 2007 Comparison of CCD, CMOS and intensified cameras. *Exp. Fluids* **42**, 403–411.

Horton, H. 1968 Laminar separation bubbles in two and three dimensional incompressible flow. PhD thesis, Department of Aeronautical Engineering, Queen Mary College, University of London.

Jeong, J. & Hussain, F. 1995 On the identification of a vortex. *J. Fluid Mech.* **285**, 69–94.

Jones, L. E., Sandberg, R. D. & Sandham, N. D. 2008 Direct numerical simulations of forced and unforced separation bubbles on an airfoil at incidence. *J. Fluid Mech.* **602**, 175–207.

Lang, M., Rist, U. & Wagner, S. 2004 Investigations on controlled transition development in a laminar separation bubble by means of LDA and PIV. *Exp. Fluids* **36**, 43–52.

Lou, W. & Hourmouziadis, J. 2000 Separation bubbles under steady and periodic–unsteady main flow conditions. *J. Turbomachin.* **122**, 634–643.

Mack, L. M. 1977 Transition prediction and linear stability theory. *AGARD* **CP 224**, 1.1–1.22.

Marxen, O., Rist, U. & Wagner, S. 2004 The effect of spanwise-modulated disturbances on transition in a 2-D separated boundary layer. *AIAA* **42**, 937–944.

Murray, M. M. & Howle, L. E. 2003 Spring stiffness influence on an oscillating propulsor. *J. Fluids Struct.* **17**, 915–926.

Ol, M. V., Hanff, E., McAuliffe, B., Scholz, U. & Kähler, C. 2005 Comparison of laminar separation bubble measurements on a low Reynolds number airfoil in three facilities. In*35th AIAA Fluid Dynamics Conf. and Exhibit*, Toronto, ON, Canada. *Paper* 2005-5149. AIAA.

Owen, P. R. & Klanfer, L. 1953 On the laminar boundary layer separation from the leading edge of a thin aerofoil. In *ARC Conf. Proc.*, p. 220.

Piirto, M., Saarenrinne, P., Eloranta, H. & Karvinen, R. 2003 Measuring turbulence energy with PIV in a backward-facing step flow. *Exp. Fluids* **35**, 219–236.

Seitz, A. & Horstmann, K. H. 2006 In-flight investigations of tollmien-schlichting waves. In *IUTAM Symposium on One Hundred Years of Boundary Layer Research. Proceedings of the IUTAM Symposium Held at DLR-Göttingen, Germany, August 12–14 2004*, pp. 115–124. Springer.

Selig, M. S., Donovan, J. F. & Fraser, D. B. 1989 *Airfoils at Low Speeds*. SoarTech.

Spalart, P. R. & Strelets, M. K. H. 2000 Mechanisms of transition and heat transfer in a separation bubble. *J. Fluid Mech.* **403**, 329–349.

Vollmers, H. 2001 Detection of vortices and quantitative evaluation of their main parameters from experimental velocity data. *Meas. Sci. Technol.* **12**, 1199–1207.

Watmuff, J. H. 1999 Evolution of a wave packet into vortex loops in a laminar separation bubble. *J. Fluid Mech.* **397**, 119–169.

Wilson, P. G. & Pauley, L. L. 1998 Two- and three-dimensional large-eddy simulations of a transitional separation bubble. *Phys. Fluids* **10**, 2932–2940.

Windte, J., Scholz, U. & Radespiel, R. 2006 Validation of the RANS-simulation of laminar separation bubbles on airfoils. *Aerosp. Sci. Technol.* **10**, 484–494.

Wissink, J. & Rodi, W. 2004 *DNS of a Laminar Separation Bubble Affected by Free-Stream Disturbances*. Springer/Kluwer Academic.